Black hole masses for 14 gravitationally lensed quasars

A. Melo, V. Motta, J. Mejía-Restrepo, R. J. Assef, N. Godoy, E. Mediavilla, E. Falco, C. S. Kochanek, F. Ávila-Vera, R. Jerez

A&A 680, A51 (2023)
https://doi.org/10.1051/0004-6361/202347078

Astronomy & Astrophysics

Black hole masses for 14 gravitationally lensed quasars

A. Melo[1,2,3], V. Motta[3], J. Mejía-Restrepo[4], R. J. Assef[5], N. Godoy[3,6,7], E. Mediavilla[8,9], E. Falco[10], C. S. Kochanek[11,12], F. Ávila-Vera[3], and R. Jerez[3]

[1] Max-Planck-Institut für Astrophysik, Karl-Schwarzschild-Str. 1, 85748 Garching, Germany
e-mail: amelo@mpa-garching.mpg.de
[2] Technical University of Munich, TUM School of Natural Sciences, Department of Physics, James-Franck-Straße 1, 85748 Garching, Germany
[3] Instituto de Físisca y Astronomía, Facultad de Ciencias, Universidad de Valparaíso, Av. Gran Bretaña 1111, Valparaíso, Chile
[4] EPAM Systems, 41 University Drive, Suite 202, Newtown, PA 18940, USA
[5] Instituto de Estudios Astrofísicos, Facultad de Ingeniería y Ciencias, Universidad Diego Portales, Av. Ejército Libertador 441, Santiago 8320000, Chile
[6] Núcleo Milenio de Formación Planetaria (NPF), 2360102, Valparaíso, Chile
[7] Aix-Marseille Univ., CNRS, CNES, LAM, Marseille, France
[8] Instituto de Astrofísica de Canarias, Vía Láctea s/n, La Laguna 38200, Tenerife, Spain
[9] Departamento de Astrofísica, Universidad de la Laguna, La Laguna 38200, Tenerife, Spain
[10] Harvard-Smithsonian Center for Astrophysics, 60 Garden Street, Cambridge, MA 02138, USA
[11] Department of Astronomy, The Ohio State University, 140 West 18th Avenue, Columbus, OH 43210, USA
[12] Center for Cosmology and Astroparticle Physics, The Ohio State University, 191 W. Woodruff Avenue, Columbus, OH 43210, USA

Received 2 June 2023 / Accepted 3 October 2023

ABSTRACT

Aims. We have estimated black hole masses ($M_{\rm BH}$) for 14 gravitationally lensed quasars using Balmer lines; we also provide estimates based on MgII and CIV emission lines for four and two of them, respectively. We compared these estimates to results obtained for other lensed quasars.
Methods. We used spectroscopic data from the Large Binocular Telescope (LBT), *Magellan*, and the Very Large Telescope (VLT) to measure the full width at half maximum of the broad emission lines. Combined with the bolometric luminosity measured from the spectral energy distribution, we estimated $M_{\rm BH}$ values and provide the uncertainties, including uncertainties from microlensing and variability.
Results. We obtained $M_{\rm BH}$ values using the single-epoch method from the Hα and/or Hβ broad emission lines for 14 lensed quasars, including the first-ever estimates for QJ0158−4325, HE0512−3329, and WFI2026−4536. The masses are typical of non-lensed quasars of similar luminosities, as are the implied Eddington ratios. We have thus increased the sample of lenses with $M_{\rm BH}$ estimates by 60%.

Key words. quasars: supermassive black holes – quasars: emission lines – gravitational lensing: strong – black hole physics

1. Introduction

Supermassive black holes (SMBHs) are thought to be a key ingredient in galaxy formation and evolution, particularly since the discovery that the central SMBH mass ($M_{\rm BH}$) has a tight correlation with the stellar luminosity and velocity dispersion (Kormendy & Richstone 1995; Ferrarese & Merritt 2000; Tremaine et al. 2002; Marconi & Hunt 2003; Kormendy & Ho 2013; Zubovas & King 2019) of the spheroidal components of their host galaxies. To understand this link, we need to study the evolution of SMBHs, their hosts, and their environments, particularly during phases with significant accretion rates when the active galactic nucleus (AGN) is releasing large amounts of energy (see, e.g., Di Matteo et al. 2005; Croton et al. 2006; Hopkins et al. 2008). Reliably measuring the $M_{\rm BH}$ is fundamental to understanding this connection.

In the unified model of AGNs (Antonucci 1993; Urry & Padovani 1995), the accretion disk continuum emission illuminates nearby gas to produce broad emission lines (BELs) in the spectra. Continuum variability drives a delayed change in the BEL fluxes and line profiles. Reverberation mapping (RM; Peterson 1993; Netzer & Peterson 1997 and therein) measures this delay to determine the size of the BEL region (Wandel et al. 1999; Kaspi et al. 2000; Peterson et al. 2004; Bentz et al. 2009), which can then be used to estimate the $M_{\rm BH}$ given the line widths and local calibrations. Even locally, RM is challenging because it requires repeated spectroscopic observations over months (Peterson et al. 2004; Bentz et al. 2009; Barth et al. 2015; Grier et al. 2017, 2019; Du et al. 2016; Lira et al. 2018), and the required monitoring periods increase for more luminous quasars or, due to time dilation, higher-redshift quasars (Lira et al. 2018). Initially, RM studies were largely limited to individual studies of local, lower-luminosity quasars, but samples have recently expanded to higher luminosities and redshifts thanks to multi-fiber spectrographs being used to monitor hundreds of AGNs simultaneously (Malik et al. 2023; Shen et al. 2023; Yu et al. 2023). Nonetheless, current RM samples have only $\sim 10^2$ AGNs, and it will be a long process to reach $\sim 10^3$ AGNs.

Fortunately, RM has revealed a correlation between the broad-line region (BLR) distance from the black hole (BH) and

the optical continuum luminosity, known as the size-luminosity relation (Kaspi et al. 2005; Bentz et al. 2006; Zu et al. 2011). This relationship, combined with the virial theorem, allows us to estimate $M_{\rm BH}$ using a single spectrum, a procedure known as the single-epoch (SE) method (e.g., McLure & Dunlop 2004; Vestergaard & Peterson 2006; Shen et al. 2011; Shen & Liu 2012). The SE method was developed and calibrated using the Hβ width (e.g., Vestergaard 2004; Xiao et al. 2011; Shen & Liu 2012). For higher-redshift systems ($z > 0.9$), Hβ is shifted into the near infrared (NIR), making it difficult to observe large samples from the ground due to the bright sky emission.

One solution is to instead use the MgII or CIV lines (McLure & Jarvis 2002; Vestergaard 2002) to study $z > 0.9$ systems in the optical (e.g., McGill et al. 2008; Park et al. 2013, 2015; Coatman et al. 2017; Woo et al. 2018). However, this approach presents several drawbacks: (1) these UV lines lack a local calibration because they cannot be observed from the ground, (2) their indirect calibrations are restricted to high-luminosity objects (Mejía-Restrepo et al. 2016), (3) MgII may have a small but significant dependence on the Eddington ratio of the AGN and might not be reliable in objects with full width at half maximum $FWHM(\mathrm{MgII}) \geqslant 6000\,\mathrm{km\,s^{-1}}$ (Marziani et al. 2013), and (4) there are concerns regarding CIV because its width could be affected by winds of ejected disk material (Assef et al. 2011; Coatman et al. 2016; Mejía-Restrepo et al. 2018) and microlensing in the case of lensed quasi-stellar objects (Fian et al. 2018a). The CIV emission line is more asymmetric than the Balmer lines and MgII, and its width is not well correlated with those of Hβ or MgII (e.g., Baskin & Laor 2005; Shen et al. 2008), but early studies showed a strong correlation between the widths of Hα, Hβ, and MgII (see Greene & Ho 2005; Shen et al. 2008; Wang et al. 2009; Shen & Liu 2012). Hence, it is reasonable to argue that the virial mass estimator based on the Balmer lines is the most reliable. The Hβ emission line is typically preferred (due to its wavelength and lack of blended emission lines), and Hα is also known to work well (Greene & Ho 2005; Netzer & Trakhtenbrot 2007; Xiao et al. 2011).

Many studies have estimated $M_{\rm BH}$ using the SE method for large samples of quasars (e.g., McLure & Jarvis 2002; McLure & Dunlop 2004; Vestergaard & Peterson 2006; Shen 2013; Peterson 2014; Mejía-Restrepo et al. 2016; Shen et al. 2019), and it has also been used to estimate $M_{\rm BH}$ for samples of lensed AGNs. Gravitational lenses offer an alternative technique for investigating the inner structure of lensed quasars (see, e.g., Kochanek 2004; Morgan et al. 2010). Despite the fact that $M_{\rm BH}$ measured in lensed quasars is affected by additional uncertainties (such as macro-model magnifications and microlensing affecting one or more images), they are crucial for extending the current SE $M_{\rm BH}$ estimation prescription at high redshifts toward lower intrinsic luminosities.

Peng et al. (2006) were the first to estimate the $M_{\rm BH}$ of gravitationally lensed AGNs. They applied the virial technique using the CIV (22 systems), MgII (19 systems), and Hβ (2 systems) emission line widths and the continuum luminosities λL_λ at 1300, 3000, and 5100 Å, respectively. Seven of the systems have estimates from two different emission lines.

Greene et al. (2010) obtained $M_{\rm BH}$ for 11 systems using Hα and/or Hβ (9 have both). Their goal was to search for systematic biases in the Peng et al. (2006) $M_{\rm BH}$ estimates due to the use of the CIV emission line. Even though the masses presented by Greene et al. (2010) are more robust (they used spectra with higher S/N), they conclude that there is no evidence for a systematic bias between the lines used by Peng et al. (2006) and the Balmer lines, despite the large scatter. Assef et al. 2011 searched for possible biases between $M_{\rm BH}$ estimates based on the Hα, Hβ, and CIV BELs, improving the sample with new observations and adding missing luminosity estimates at λ = 5100 Å. They selected 12 lensed quasars from the CfA-Arizona Space TElescope LEns Survey (CASTLES[1]; Falco et al. 2001) with high-quality CIV spectra and published NIR spectra of the Balmer lines. The FWHMs were obtained using broad and narrow Gaussian components, and the continuum luminosity at 5100 Å was estimated using the AGN spectral energy distribution (SED) template from Assef et al. (2010). They conclude that the $M_{\rm BH}$ inferred from CIV using the line dispersion (σ_l) shows a systematic offset with respect to the estimate based off the FWHM. However, Assef et al. (2011) compared the $M_{\rm BH}$ estimated using CIV and the Balmer lines and found no significant offset. Sluse et al. (2012), in a study of microlensing involving a sample of 17 lensed quasars, obtained $M_{\rm BH}$ using the CIV (5 systems), MgII (12 systems), and Hβ emission lines (2 systems); 2 of the 17 systems had estimates from two different emission lines, and 4 had published values from Peng et al. (2006) and Assef et al. (2011).

Before our study, no new $M_{\rm BH}$ estimates had been obtained for lensed quasars for a decade. In general, recent publications refer to the $M_{\rm BH}$ mentioned above (e.g., Ding et al. 2017a, 2021; Guerras et al. 2020; Hutsemékers & Sluse 2021), and only 14 of the 222[2] known lensed quasars have $M_{\rm BH}$ measurements based on the Hα and/or Hβ lines. In this work, we increase the sample of Balmer line $M_{\rm BH}$ estimates for lensed AGNs from 14 to 23 sources. Even though the objects in our sample (with the exception of WFI2026−4536 and HE0512−3329) have BH mass estimates (Peng et al. 2006; Assef et al. 2011; Sluse et al. 2012; Ding et al. 2017a), only two of them (SDSS1138+0314 and HE1104−1805) were obtained using Hα or Hβ. Most are based on the CIV and/or MgII BELs. We also include three quasars with no previous $M_{\rm BH}$ estimates.

This paper is structured as follows. In Sect. 2 we present the systems and data reduction for the three different instruments used in this work (VLT/X-shooter, LBT/LUCI, and *Magellan*/MMIRS). Section 3 describes the method for obtaining $M_{\rm BH}$ and the factors that could contribute to its uncertainties. Our results are presented in Sect. 4, where we analyze the systems and compare them with the large samples of non-lensed AGNs. Finally, our conclusions are presented in Sect. 5. Throughout the paper we assume a Λ cold dark matter cosmology with $\Omega_\Lambda = 0.7$, $\Omega_M = 0.3$, and $H_O = 70\,\mathrm{kms^{-1}\,Mpc^{-1}}$.

2. Observations and data reduction

We present observations for three systems with the X-shooter instrument (Vernet et al. 2011) and one observation with the FOcal Reducer/low dispersion Spectrograph 2 (FORS2; Rupprecht & Böhnhardt 2000) at the Very Large Telescope (VLT). In addition, we include 21 spectroscopic observations taken in 2012 for 14 lensed quasars with the Large Binocular Telescope (LBT) and the LUCI spectrograph (Seifert et al. 2003) or the *Magellan* telescope and the MMT and *Magellan* Infrared Spectrograph (MMIRS; McLeod et al. 2012). Table 1 summarizes the main observational characteristics for the observing runs, the image(s) observed for each lensed quasar and the

[1] https://lweb.cfa.harvard.edu/castles/

[2] Gravitationally Lensed Quasar Database, GQL https://research.ast.cam.ac.uk/lensedquasars/index.html

Table 1. Observations.

Object	Date (dd-mm-YYYY)	Position angle (°)	Exp. time (s)	Image(s)	Band	Inst.
HE0047−1756	25-Nov-2012	354.121	120	A	HKspec	LUCI
HE0047−1756	25-Nov-2012	354.121	120	A	*J*	LUCI
HE0435−1223	27-Nov-2012	303.674	120	A	HKspec	LUCI
HE0512−3329	06-Apr-2012	85.409	180–300	A-B	HK	MMIRS
SDSS0924+0219	24-Nov-2012	361.326	120	A	HKspec	LUCI
SDSS0924+0219	24-Nov-2012	361.326	600	A	*J*	LUCI
Q1017−207				A-B	HK	MMIRS
HE1104−1805	07-Apr-2012	131.361	180–300	A-B	HK	MMIRS
SDSS1138+0314	06-Apr-2012	93.836	180–300	A-B	HK	MMIRS
SDSSJ1335+0118	07-Apr-2012	90.246	180–300	A-B	HK	MMIRS
WFI2026−4536	06-Nov-2012	19.798	180	A-B	HK	MMIRS
WFI2033−4723	06-Apr-2012	59.148	180–300	C-A2	HK	MMIRS
HE2149−2745	06-Apr-2012	38.578	180–300	A-B	HK	MMIRS
QJ0158−4325	21/22-Aug-2019	70.98	600 × 8	A-B	UVB, VIS and NIR	X-shooter
QJ0158−4325	19/20-Sep-2019	70.98	600 × 8	A-B	UVB, VIS and NIR	X-shooter
SDSS1226−0006	6/7-Mar-2013	87.5	600 × 4	A-B	UVB, VIS and NIR (JH)	X-shooter
SDSS1226−0006	10/13-Feb-2010	−91.89	2800 × 4	A-B	VIS	FORS2
LBQS1333+0113	27/28-Feb-2020	138.439	600 × 8	A-B	UVB, VIS and NIR	X-shooter
LBQS1333+0113	28/29-Feb-2020	138.439	600 × 8	A-B	UVB, VIS and NIR	X-shooter
Q1355−2257	28/29-Feb-2020	−106.467	600 × 8	A-B	UVB, VIS and NIR	X-shooter
Q1355−2257	6/7-Apr-2021	−106.467	600 × 8	A-B	UVB, VIS and NIR	X-shooter

orientation of the slit. Data reduction for each instrument is described below.

2.1. X-shooter

LBQS1333+0113, QJ0158−4325, and Q1355−2257 were observed with X-shooter between August 2019 and April 2021 (ESO proposal ID 103.B − 0566(A); PI: A. Melo). We used two observing blocks (OBs) for each system with a slit width of 1.″0 × 11″ for the UVB band (resolution of R = 5400) and 1.″2 × 11″ for the VIS and NIR arms (R = 6500 and 4300, respectively). In the first OB, four exposures were taken in the NIR arm (600s each) and two exposures in the VIS and UVB arms (600s each), with a nodding of 3″ per frame and a read-out mode (UVB and VIS) of 100k/1pt/hg. The second OB had the same configuration as the first one, but the NIR data were taken with two exposures instead of four. The slit was centered on the brightest image of the lensed quasar and the position angle was chosen to include the second brightest image. We used the atmospheric dispersion corrector to correct for differential atmospheric refraction. SDSS1226−0006 was observed in 2013, with slit width of 1.″6 × 11″ for the UVB band, 1.″5 × 11″ for VIS and 0.″9 × 11″ NIR arm.

The data were reduced using the European Southern Observatory (ESO) pipeline `EsoReflex` (Freudling et al. 2013) along with the principal component analysis (PCA) method (Deeming 1964; Bujarrabal et al. 1981; Francis & Wills 1999) for the sky emission subtraction. We briefly summarize the steps here (more details can be found in Melo et al. 2021). First, X-shooter pipeline version 3.5.0 of `EsoReflex` was used to reduce each individual OB (flat field, dark current, wavelength calibration, among others) without correction for nodding and without subtracting the sky background. We used PCA for the sky emission correction in the NIR on each individual frame. First, we masked outliers (such as bad pixels) using σ-clipping and replace them with a value from a bicubic interpolation of the surrounding pixels. We calculated a sky median as a function of wavelength, subtract it from each frame and collapse the two-dimensional spectra along the wavelength axis to select an uncontaminated spatial region for the sky emission. We chose the PCA-basis as the region of threshold equal to 3 of the median above the background (see Fig. 2 of Melo et al. 2021). Finally, we constructed a model of the sky emission in the selected spatial region as our PCA eigenvector basis and subtracted it from the frame.

Flux calibration was done using Eq. (3) of the X-shooter Pipeline User Manual[3] with the response curve from the X-shooter pipeline based on a standard star observed the same night as the target. We used `molecfit` (Smette et al. 2015; Kausch et al. 2015) for the telluric correction of each spectrum and employed the best fit to each spectrum row by row. Finally, the spectra were median combined using the parameters from the header for the stacking. The uncertainties were estimated as the median absolute deviation. For the VIS and UVB reduction, we used a median of each sky region as the model of the sky brightness but otherwise followed the same steps used for the NIR.

2.2. LUCI

The systems HE0047−1756, HE0435−1223, SDSS0924+0219, and Q1017−207 were observed (November 24-27, 2012) in the long-slit mode using the gratings 200_H+K (with a resolving power of 1881 at H and 2573 at K) and 210_zJHK (a resolving power of 6877, 8460, 7838, and 6687 at z, J, H, and K, respectively) with a 0.″5 wide slit. The N1.8 camera was used with a pixel scale of 0.″25. The estimated seeing was ∼0.″8.

Data reduction was performed using the Image Reduction and Analysis Facility (IRAF) packages along with Interactive Data Language (IDL) task `xtellcor_general` from Vacca et al. (2003) for the telluric absorption correction. The

[3] https://ftp.eso.org/pub/dfs/pipelines/instruments/xshooter/xsh-pipeline-manual-12.1.pdf

detailed reduction is described in Assef et al. (2011), but we present a summary of the steps here. For each exposure, a two-dimensional wavelength calibration was performed using the sky emission lines, and a combined median sky frame was built. This sky frame was used to remove the sky before extracting the spectra. The telluric absorption correction was made using `xtellcor_general`.

2.3. MMIRS

Seven lensed systems were observed using MMIRS April 6-7, 2012, using the long-slit data spanning H/K bands (1.25–2.4 μm). Two images of the lensed quasar were positioned in a slit of 0.″8 wide with a pixel scale of 0.″2012[4]. The spectra were taken with nodding to control for the sky background.

Data reductions were carried out with the instrument pipeline (Chilingarian et al. 2015) and IRAF[5] tasks. The code `mmfixall`, provided by the MMIRS instrument scientific team, was used to collapse the information contained in the multi-extension files. The remaining procedures were performed in IRAF and consisted of dark correction, sky subtraction, one-dimensional spectra extraction, wavelength calibration and telluric correction. The one-dimensional spectra was extracted using the `apall` task with apertures of ±3−4 pixels. Flux calibration was carried out using `xtellcor_general` for telluric absorption corrections.

2.4. FORS2

Only SDSS1226−0006 was observed using FORS2 in February 2010. Data reduction was performed using IRAF and standard procedure consisting of bias subtraction and flat fielding, including the rejection of cosmic rays. The spectra were extracted using the apall task, setting two apertures and fixing the centroid of each quasar spectra.

3. Method

As discussed earlier, the SE method combines the BLR line width and size determined from the luminosity to estimate

$$M_{\rm BH} = f\frac{R_{\rm BLR}(\Delta v)^2}{G}, \quad (1)$$

where $R_{\rm BLR}$ is the distance from the SMBH to the BLR, Δv is the virial velocity of the BLR, G is the gravitational constant and f is the virial factor that depends on the unknown kinematics, structure, inclination, and distribution of the BLR (Peterson et al. 2004 and references therein). Since the emission lines may originate under different conditions, the f parameter may differ between quasars (Shen 2013), which in turn gives rise to one of the main uncertainties in measuring $M_{\rm BH}$. The virial factor has been estimated (e.g., Collin et al. 2006; Woo et al. 2015; Mediavilla et al. 2020) from different emission lines. In this paper we assume $f = 1$ following the results of Woo et al. (2015), which is in agreement with the non-weighted average $\langle f \rangle = 0.99 \pm 0.08$ of Mediavilla & Jiménez-Vicente (2021). Thanks to the known correlation between the luminosity of the AGN and the size of the BEL (e.g., Kaspi et al. 2000, 2005; Bentz et al. 2009), and assuming viral equilibrium, we estimated the mass as

$$\log(M_{\rm BH}/M_\odot) = \log(K) + \alpha \log\left(\frac{\lambda L_\lambda}{10^{44}\,{\rm erg\,s^{-1}}}\right) + 2.0 \log\left(\frac{FWHM}{1000\,{\rm km\,s^{-1}}}\right), \quad (2)$$

where

$$(\log K, \alpha)_{\rm H\alpha} = (6.845, 0.650),$$
$$(\log K, \alpha)_{\rm H\beta} = (6.740, 0.650),$$
$$(\log K, \alpha)_{\rm MgII} = (6.925, 0.609), \text{ and}$$
$$(\log K, \alpha)_{\rm CIV} = (6.353, 0.599)$$

are the calibrated parameters from Mejía-Restrepo et al. (2018) for the Hα, Hβ, MgII, and CIV lines, respectively, and the luminosities are those at 5100 Å (L_{5100}) for Hα and Hβ, 3000 Å (L_{3000}) for MgII, and 1450 Å (L_{1450}) for CIV.

3.1. Emission line fitting

We modeled the emission line profiles after removing the continuum and an iron line template, following Mejía-Restrepo et al. (2016). We used a maximum of two Gaussian broad components and a single narrow line component for each emission line. In addition to the narrow and broad components of the principal emission lines (Hα, Hβ, CIV and MgII), we added four extra components in the Hα profile for the [N II] and [S II] narrow-line doublets, two for the [O III] narrow-line region (NLR) doublet in the Hβ profile plus one to the He II BEL. We masked regions with telluric absorption problems, bad seeing and poor S/N that could affect our fit. The best final fit is shown as a red line in Fig. 1 for the LUCIFER and MMIRS data, and in Figs. 2–5 for QJ0158−4325, LBQS1333−0113, Q1355−2257, and SDSS1226−0006, respectively. In the cases using two BELs, the FWHM was calculated from the combined profile after removing the NLR components. We carried out a Monte Carlo simulation consisting of 1000 simulated spectra randomly adding the estimated spectral noise to obtain a 95% confidence uncertainty estimate.

3.2. Luminosity measurements

We followed Assef et al. (2011) and estimated the monochromatic luminosity of each quasar using the broadband SED of the brightest image (A) and the fluxes from CASTLES and other sources in the literature (see Table A.1). If we obtained a useful spectrum of the fainter image, we also modeled its SED. This method was preferred over using the continuum obtained from the spectra due to several factors affecting the LUCIFER and MMIRS data (e.g., low S/N (3–18), unresolved images in the slit, seeing conditions varying between the target and the standard star) and because of the chromatic microlensing detected in the continuum of the four systems observed with X-shooter and FORS2 (Melo et al., in prep.). To demagnify the fluxes, we used the magnification estimated from a lens model (Table 2). We chose photometric data that were obtained close in time to our observations to minimize differences in the amount of microlensing or a large intrinsic variation that coupled with the time delay could mimic chromatic microlensing. If light curves were available, we included the variability amplitude as part of the flux

[4] https://lweb.cfa.harvard.edu/mmti/mmirs/instrstats.html

[5] IRAF is distributed by the National Optical Astronomy Observatory, which is operated by the Association of Universities for Research in Astronomy, Inc., under cooperative agreement with the National Science Foundation.

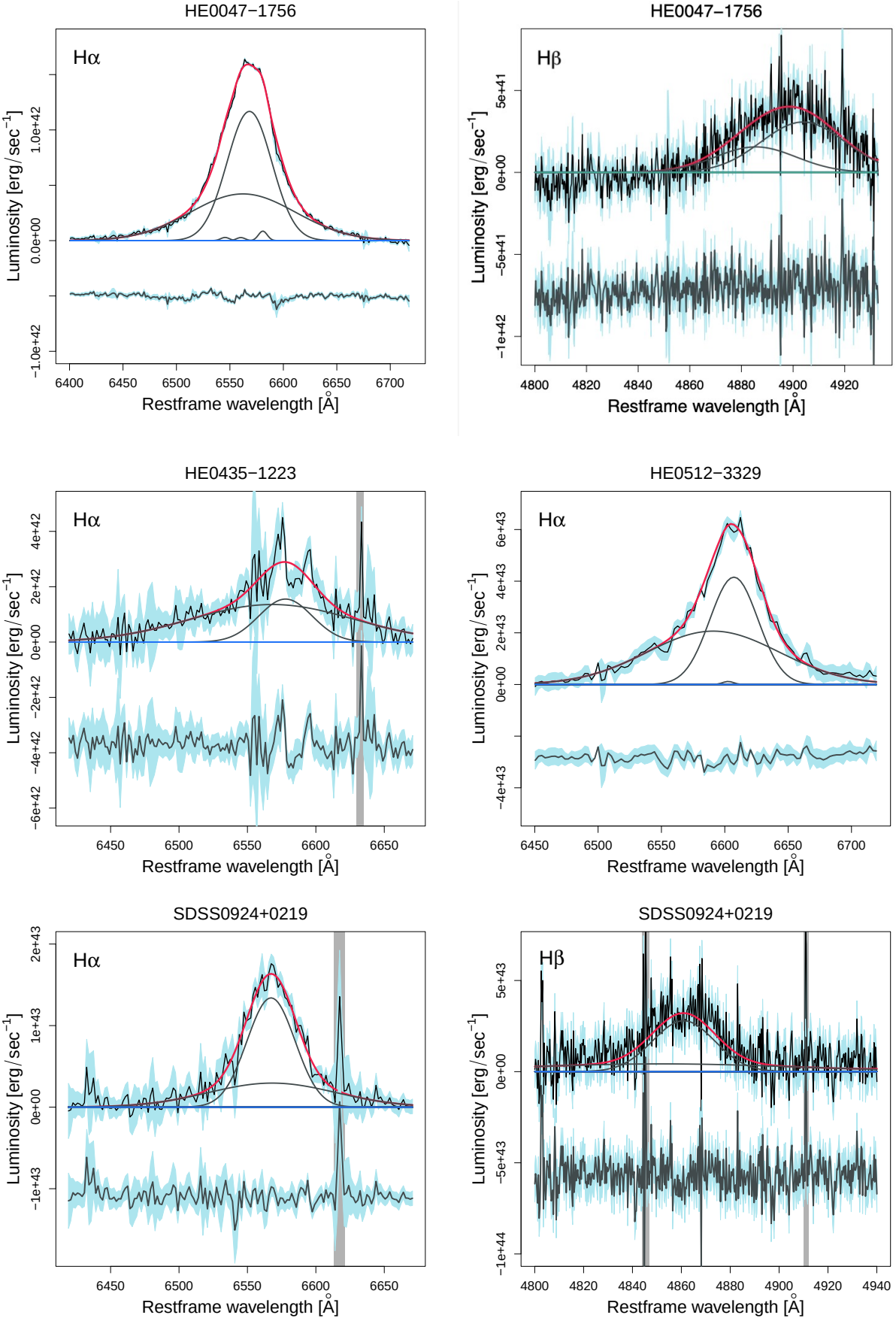

Fig. 1. Gaussian fits to the Hα and Hβ lines of the lensed systems. The red line is the best fit, the black lines are the different components of each region (emission and absorption), the green line is the Fe template, and the blue line is the continuum fit. The 1-sigma errors are shown by the blue regions, and the model residuals are shown below each spectrum.

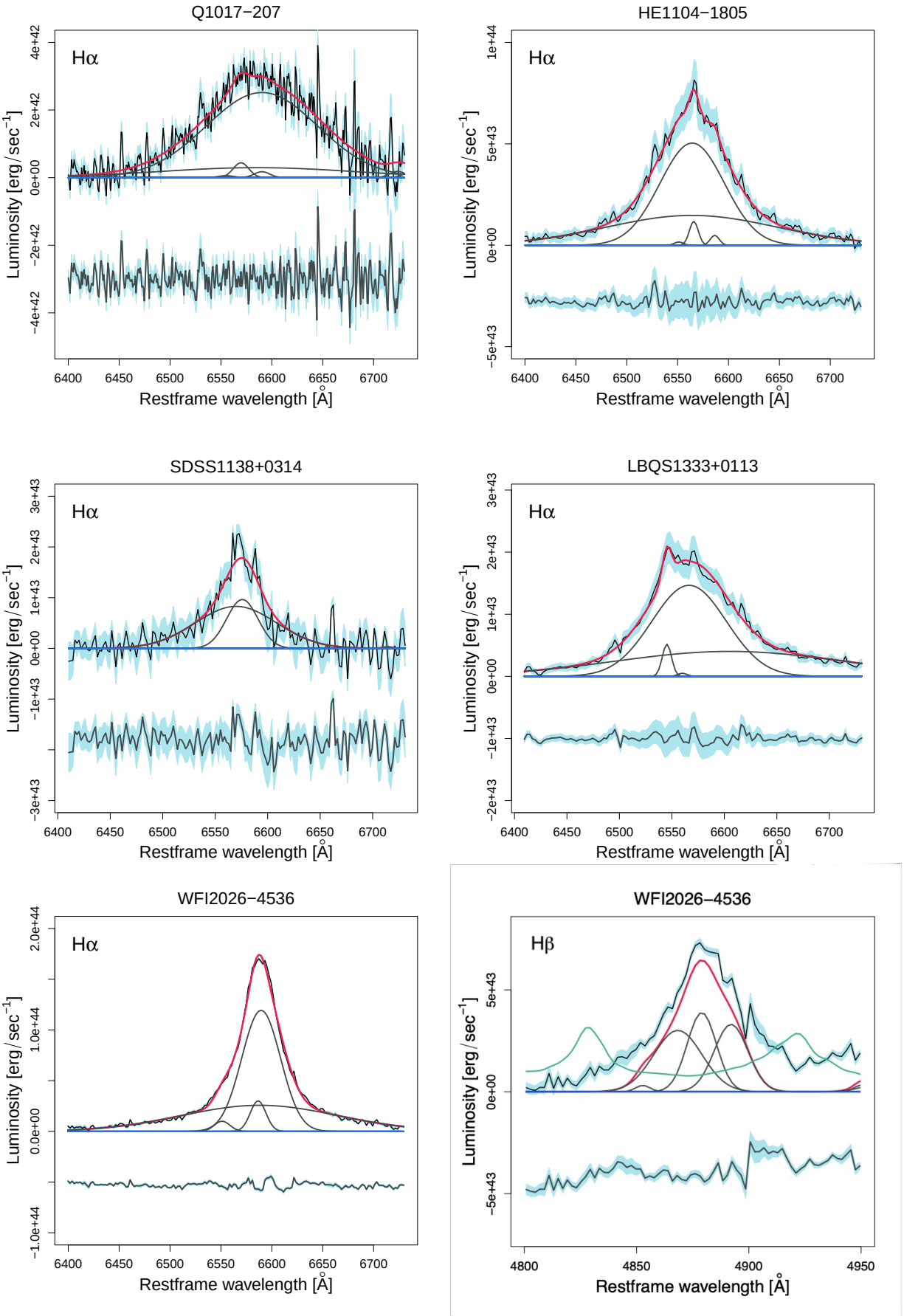

Fig. 1. continued.

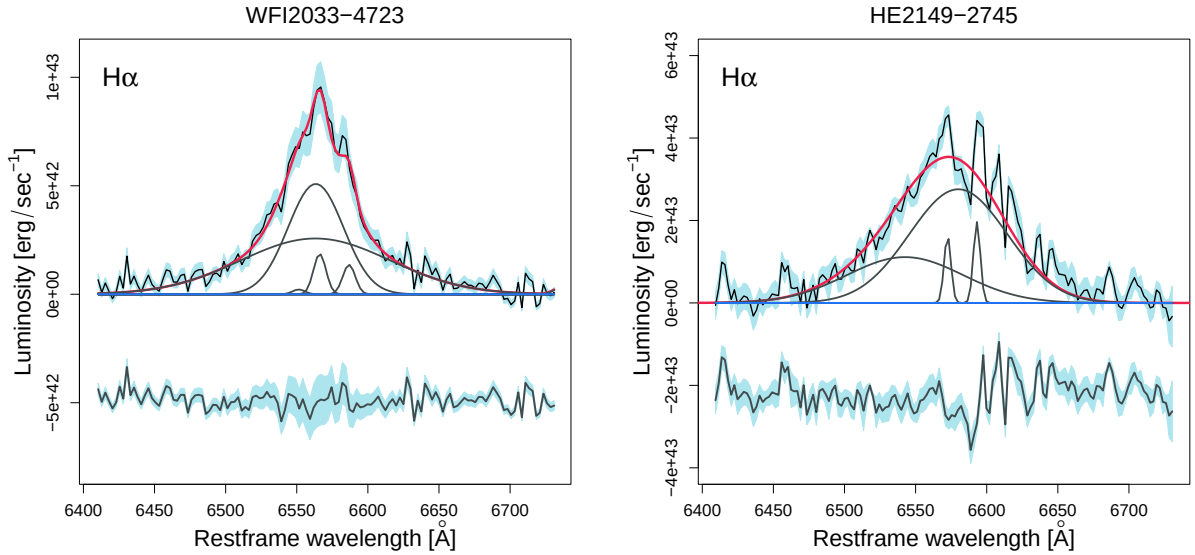

Fig. 1. continued.

uncertainties. For instance, Giannini et al. (2017) demonstrated that HE0047−1756 varied by ∼0.2–0.3 mag over a five-year period, and WFI2033−4723 varies by 0.5 mag in four years. The system HE0435−1223 varied ∼0.4 mag (Ricci et al. 2011) and more recently, Bonvin et al. (2017) presented 13-yr light curves with a variability amplitude of ∼0.7 mag.

3.3. Uncertainties

We needed to consider multiple factors that could contribute to the uncertainties in $M_{\rm BH}$. For example, the BEL of one of the images could be microlensed (e.g., microlensing affecting the red wing of the Hα emission line in HE0435−1223, Braibant et al. 2014, and the blue wing of MgII for the same system in Fian et al. 2018a), leading to a larger FWHM. Melo et al. (2021) showed that even if we have a FWHM difference between the images of >5 sigma, the impact on $M_{\rm BH}$ is negligible compared with other sources of errors (see below for a specific example).

Another contribution to the uncertainties is the blending of the images in some of the MMIRS spectra. To see how much this could affect the $M_{\rm BH}$, we compared the FWHM we found from fitting the blended image A+B spectrum of LBQS1333+0113 to the separate spectra of the two images (see Fig. 6). For Hα the FWHM of the combined spectrum is $4750 \pm 110\,{\rm km\,s^{-1}}$ compared to $4610 \pm 70\,{\rm km\,s^{-1}}$ for image A and $4755 \pm 24\,{\rm km\,s^{-1}}$ for image B. These differences translate to estimated masses of $\log_{10}(M_{\rm BH}/M_\odot) = 9.16 \pm 0.59$, 9.13 ± 0.54, and 9.16 ± 0.48, which are much smaller than the other sources of error and thus unimportant for the BH mass estimate. A similar result is obtained for the MgII line.

Another factor contributing to the error is the monochromatic luminosity uncertainty. This has several systematic uncertainties: the systematic errors of the instrument, the magnification of the image given by the lens model, the flux calibration and intrinsic variability. To account for the intrinsic AGN variability, we added the observed variability as a contribution to the error in the monochromatic luminosity (Sect. 3.2). Although the uncertainties in the luminosity are large, the $M_{\rm BH}$ estimate scales as $L^{1/2}$, making it less sensitive to these errors compared to the FWHM because the $M_{\rm BH} \propto FWHM^2$ is so much stronger.

4. Results

Using the FWHM from the models of the emission lines and the monochromatic luminosity obtained from the SEDs, we measured $M_{\rm BH}$ following Eq. (2). The results are shown in Table 3 along with their respective errors. Two systems have previous Hα $\log_{10}(M_{\rm BH}/M_\odot)$ (Assef et al. 2011): HE1104−1805 (9.05 ± 0.23) and SDSS1138+0314 (8.22 ± 0.22), respectively. Our estimate for HE1104−1805 is in agreement given its error (8.87 ± 0.70), while for SDSS1138+0314 the result is 0.27 dex smaller (7.95 ± 0.50). The difference in this case is due to a combination of factors: (1) we obtain a smaller FWHM ($2330 \pm 138\,{\rm km\,s^{-1}}$ versus $4700 \pm 200\,{\rm km\,s^{-1}}$), (2) a lower luminosity ($\log_{10}(L_{5100}) = 44.57 \pm 0.31$) versus $\log_{10}(L_{5100}) = 44.81$, 3), (3) a low S/N (∼10 for the spectra of image A in this work versus ∼8 for presented in Assef et al. 2011).

These are the first $M_{\rm BH}$ estimates obtained for the systems QJ0158−4325 ($\log_{10}(M_{\rm BH}/M_\odot) = 8.05 \pm 0.58$, 8.51 ± 0.25, and 8.32 ± 0.46 for CIV, MgII, and Hα, respectively), HE0512−3329 ($\log_{10}(M_{\rm BH}/M_\odot) = 8.14 \pm 0.25$), and WFI2026−4536 ($\log_{10}(M_{\rm BH}/M_\odot) = 8.28 \pm 0.25$ and 7.83 ± 0.35, for Hα and Hβ, respectively).

The systems HE0047−1756, HE0435−1223, SDSS0924+0219, SDSS1226−0006, LBQS1333+0113, Q1355−2257, and WFI2033−4723 have previous estimates of $M_{\rm BH}$, which were made using the MgII emission lines (Peng et al. 2006; Sluse et al. 2012; Ding et al. 2017b), and we compared these estimates to our Balmer lines estimates in Fig. 7. Lensed quasars that have one or both $M_{\rm BH}$ estimates presented in this work are shown in color. In general, our estimates are well correlated after we apply the offset of Mejía-Restrepo et al. (2016; 0.16 dex for $M_{\rm BH}$ measured with Hα, and 0.25 dex using MgII). The systems in which the $M_{\rm BH}$ differ for both lines (FBQ0951+2635, B1422+231, and Q2237+030) were obtained by different authors using different methods (Assef et al. 2011; Sluse et al. 2012) and different epochs.

The left panel of Fig. 8 shows the distribution in $M_{\rm BH}$ and $L_{\rm bol}$ for our systems along with estimates from the literature for 34 lensed quasars (Peng et al. 2006; Greene et al. 2010; Assef et al. 2011; Sluse et al. 2012; Melo et al. 2021). Figure 8 (right) shows the distribution in luminosity and BH mass only considering the estimates from the Balmer lines.

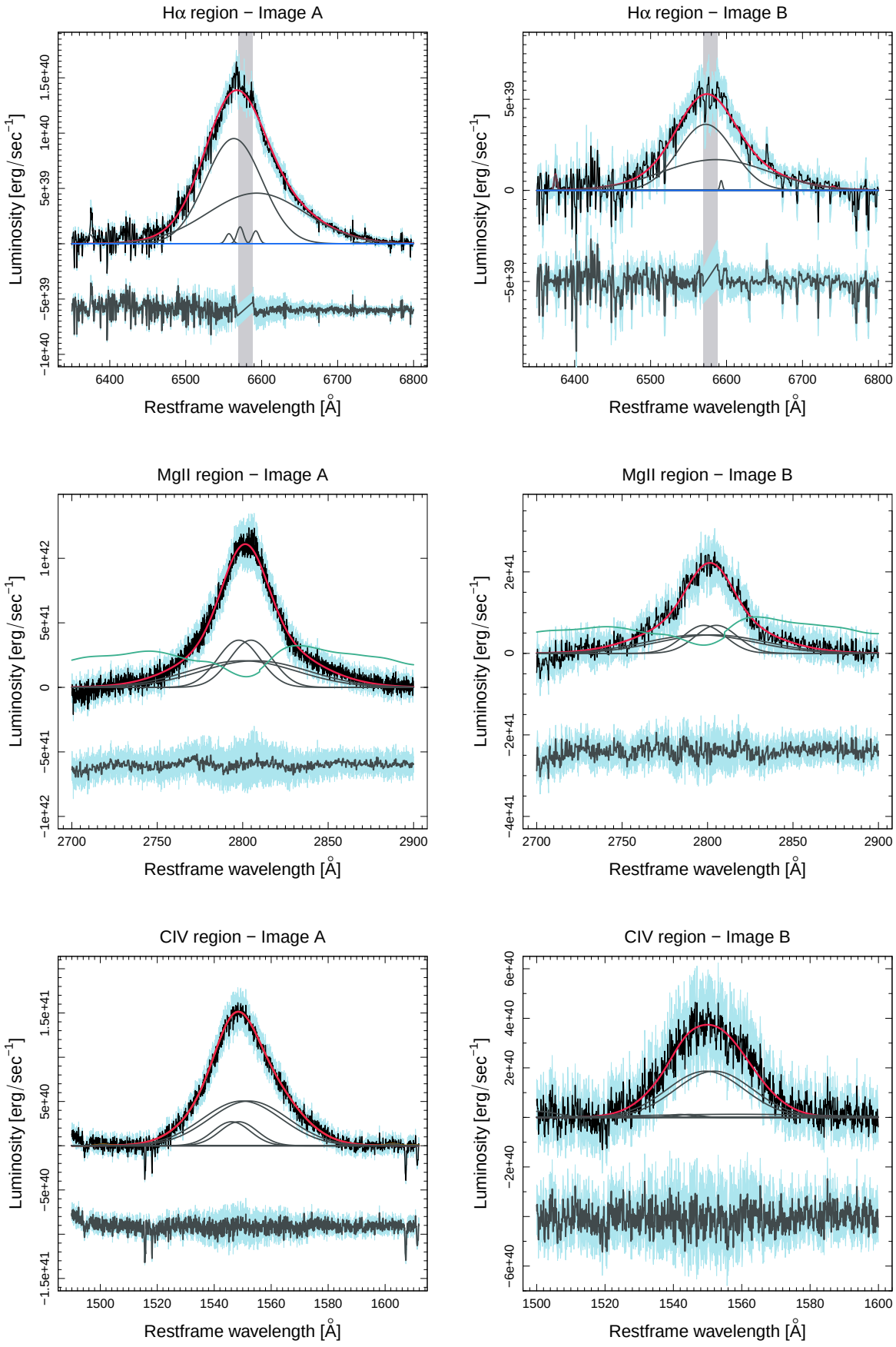

Fig. 2. Gaussian fits to the A and B image BELs of QJ0158-4325. The red line is the best fit, the black lines are the different components of each region (emission and absorption), the green line is the Fe template, and the blue line is the continuum fit. The 1-σ errors are shown by the blue regions, and the model residuals are shown below each spectrum.

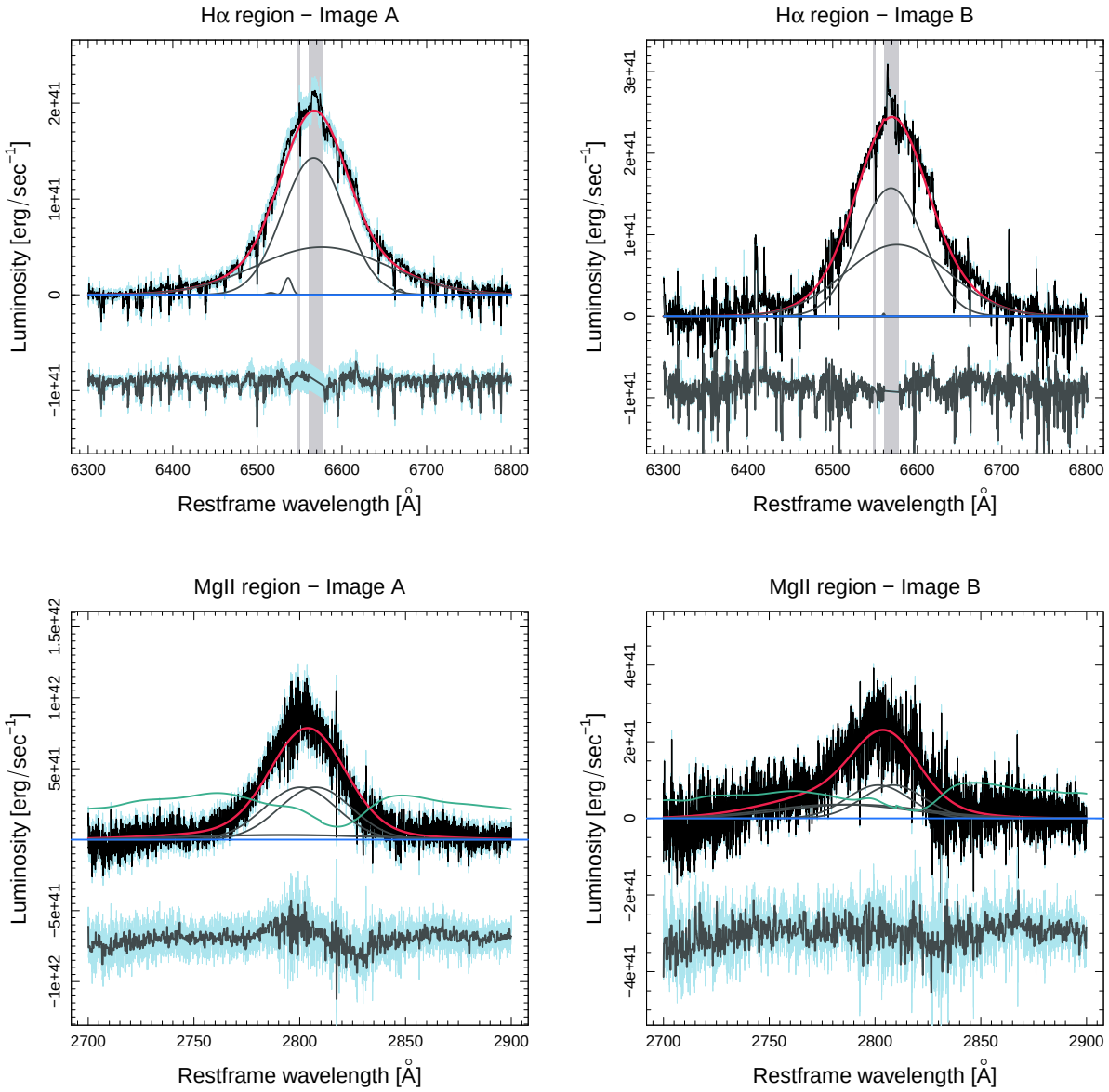

Fig. 3. Same as Fig. 2 but for LBQS1333+0113.

The Eddington ratios of the lensed quasars are typically close to ∼0.1, which agrees with the results from Shen et al. (2019) based on SE virial BH masses of quasars. Some of the systems have several values obtained from different emission lines. The intrinsic luminosity was converted to bolometric using $L_{\rm bol} = A \times L_{\rm ref}$, where $A = (3.81, 5.15, 9.6)$ for $L_{\rm ref} = (L_{1350}, L_{3000}, L_{5100})$ from Sluse et al. (2012). $M_{\rm BH}$ values obtained for non-lensed quasars using the SE method by Shen et al. (2019) are included as the contoured distribution for comparison. In general, the new $M_{\rm BH}$ obtained from the Balmer lines span the same range of masses as the lensed and non-lensed AGNs (Fig. 8). In particular, we were able to obtain estimates for the lower-luminosity systems QJ0158−4325, SDSS0924+0219, HE0512−3329 and HE0047−1756 (from 10^{44} to $10^{46.5}$). The systems QJ0158−4325 and SDSS0924+0219 have the lowest luminosities ($\log_{10}(L_{\rm ref}) < 44.60\ L_{\odot}$), and the latter has the lowest $M_{\rm BH}$, $\log_{10}(M_{\rm BH}/M_{\odot}) = 7.43 \pm 0.05$ (this is the average of the Hα and Hβ estimates).

We separately examined the three systems observed with X-shooter (QJ0158−4325, LBQS13333+0113, and Q1355−2257) because they have multiple $M_{\rm BH}$ estimates using different emission lines. The SEDs were obtained independently for both images (A and B; see Table A.1), and the results show that the estimated magnification-corrected luminosity and $M_{\rm BH}$ are in good agreement within the estimated errors.

In the case of LBQS1333+0113, we only used Hα and MgII because CIV line exhibits multiple absorption features and Hβ has low S/N (Melo et al., in prep). MgII and Hα are in good agreement with mean values of $\log_{10}(M_{\rm BH}/M_{\odot}) = 9.25 \pm 0.51$, and 9.01 ± 0.91, respectively. The FWHM of the Hα emission line observed with MMIRS is in agreement given its errors with that obtained with X-shooter. Sluse et al. (2012) obtained $M_{\rm BH}$ from the MgII ($\log_{10}(M_{\rm BH}/M_{\odot}) = 9.19 \pm 0.26$), which agrees with our X-shooter result. Q1355−2257 exhibits a wide range of mass estimates depending on the emission line with mean values of $\log_{10}(M_{\rm BH}/M_{\odot}) = 8.20 \pm 0.71$, 9.12 ± 0.35 and 8.77 ± 0.88 for CIV, MgII, and Hα, respectively (green

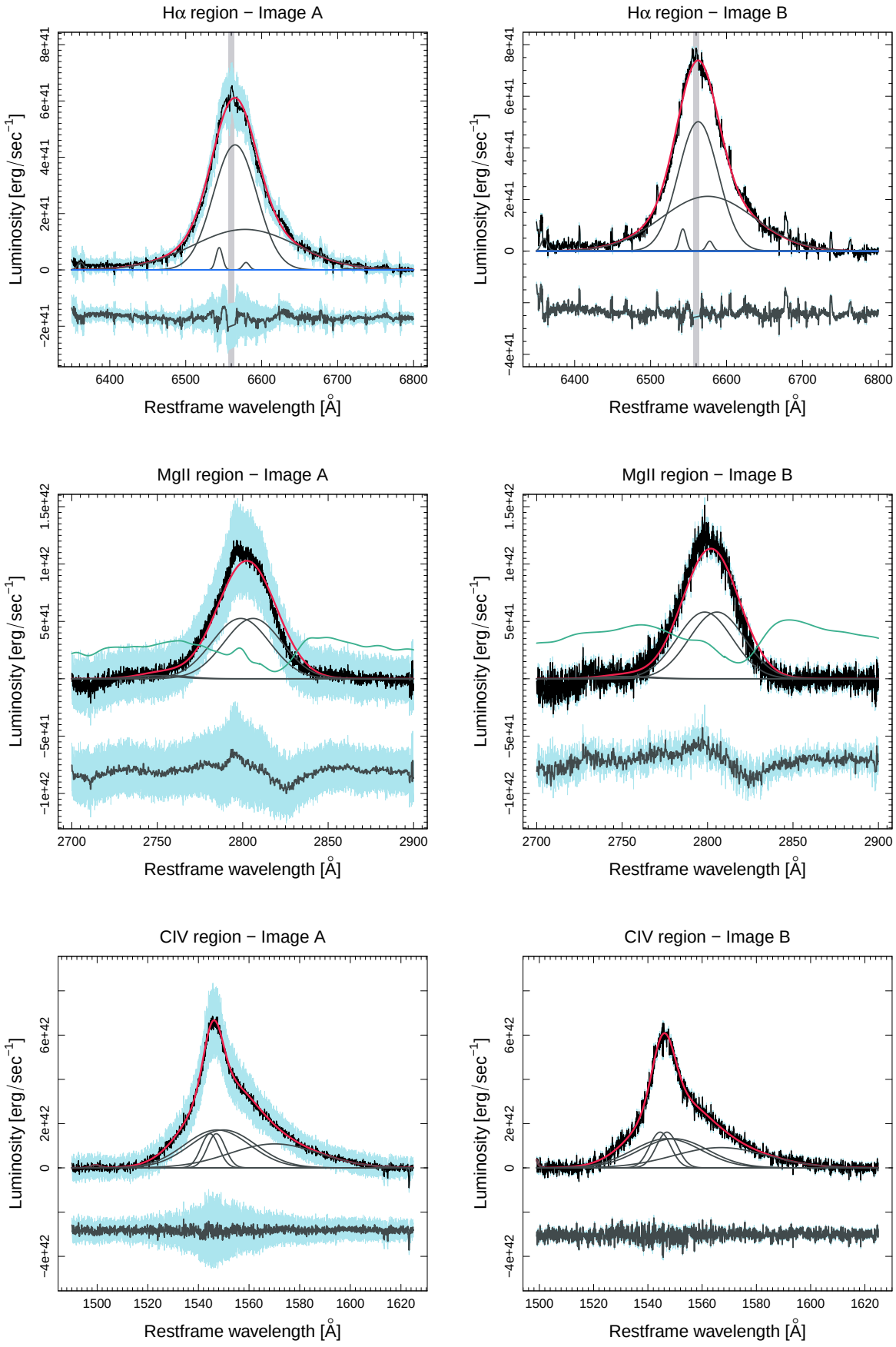

Fig. 4. Same as Fig. 2 but for Q1355−2257.

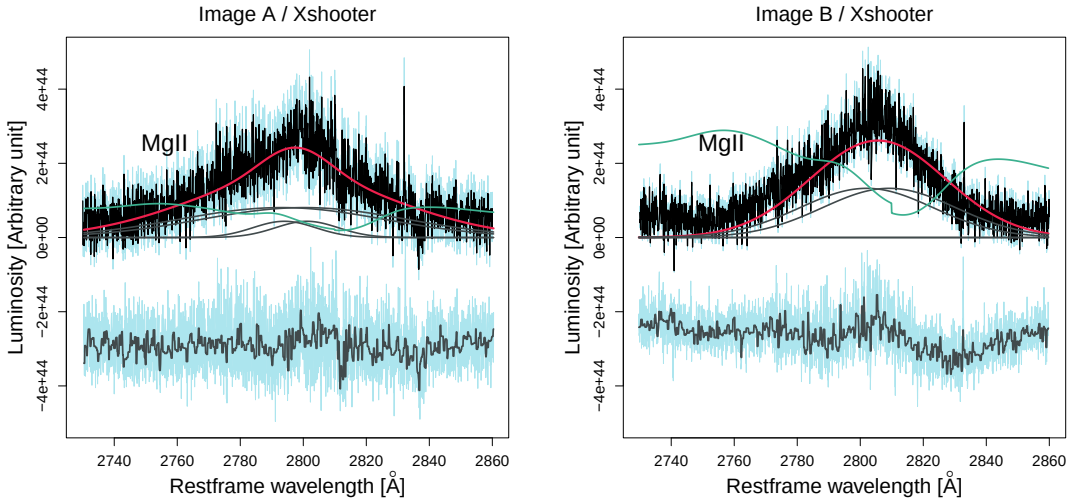

Fig. 5. Same as Fig. 2 but for SDSS1226−0006.

Table 2. Magnification values used for demagnifying the flux and their references.

Object	z_s	Magnification	Image	Ref.
HE0047−1756	1.66	13.87	A	Rojas et al. (2014)
QJ0158−4325	1.29	25.27	A	Bhatiani et al. (2019)
QJ0158−4325	1.29	12.32	B	Bhatiani et al. (2019)
HE0435−1223	1.689	7.27	A	Fian et al. (2018b)
HE0512−3329	1.57	7.44	A	Mediavilla et al. (2009)
SDSS0924+0219	1.524	21.05	A	Mediavilla et al. (2009)
Q1017−207	2.55	4.54	A	Mediavilla et al. (2009)
HE1104−1805	2.32	16.20	A	Assef et al. (2011)
SDSS1138+0314	2.44	7.30	A	Eigenbrod et al. (2006)
SDSS1226-0006	1.12	3.83	A	Sluse et al. (2012)
SDSS1226-0006	1.12	3.07	B	Sluse et al. (2012)
LBQS1333+0113	1.57	3.77	A	Sluse et al. (2012)
LBQS1333+0113	1.57	0.87	B	Sluse et al. (2012)
Q1355−2257	1.37	2.50	A	Sluse et al. (2012)
Q1355−2257	1.37	0.85	B	Sluse et al. (2012)
WFI2026−4536	2.23	14.20	A1	Bate et al. (2018)
WFI2033−4723	1.66	3.13	A	Sluse et al. (2012)
HE2149−2745	2.03	2.71	A	Sluse et al. (2012)

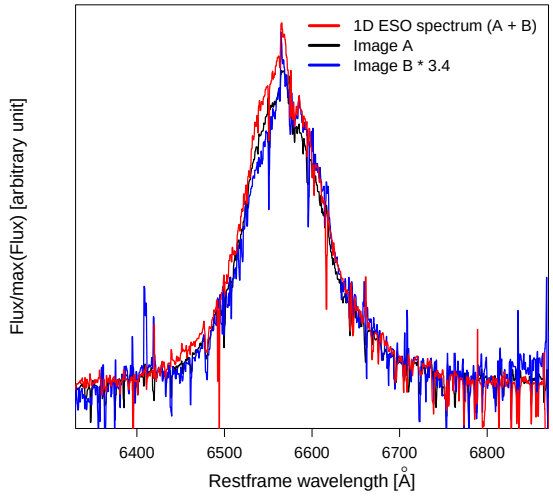

Fig. 6. Combined spectra of images A+B (red spectra), compared to image A (black spectra) and image B (blue spectra) for the system LBQS1333+0113. We subtracted the continuum for the three spectra and multiplied image B by a factor of 3.4 for a clearer comparison.

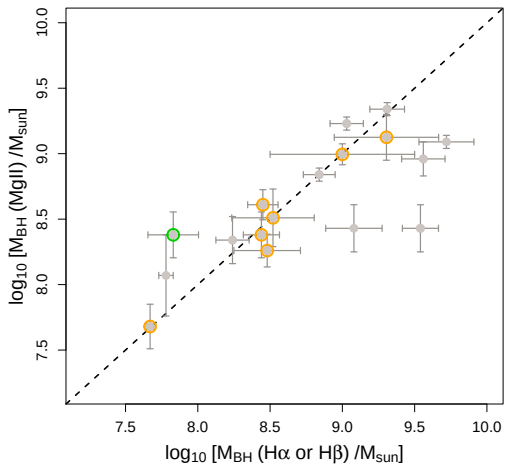

Fig. 7. Comparison between M_{BH} estimates obtained from the Balmer lines and MgII emission lines. The new measurements are marked in orange (Hα emission line) and green (Hβ emission line). The systematic offset from Mejía-Restrepo et al. (2016) is applied. The dotted line shows where the masses are equal.

Table 3. Hα and Hβ mass estimates of the observed images.

Image	Line	*FWHM* [km s^{-1}]	$\log_{10}(L_{\rm ref})$ [a] [erg s^{-1}]	$\log_{10}(M_{\rm BH})$ [$M_\odot$]	$\log_{10}(r_{\rm s})$ [b] [cm]	*S*/*N*
MMIRS and LUCIFER						
HE0047−1756	Hα	2678 ± 37	44.92 ± 0.56	8.29 ± 0.21	15.44 ± 0.85	28.11
HE0047−1756	Hβ	2719 ± 317	44.92 ± 0.56	8.20 ± 0.50	15.21 ± 0.47	5.9
HE0435−1223	Hα	3216 ± 579	44.77 ± 0.01	8.36 ± 0.57	15.49 ± 0.42	3.7
HE0512−3329	Hα	2629 ± 10	44.71 ± 0.92	8.14 ± 0.25	15.34 ± 0.77	12.6
SDSS0924+0219	Hα	2127 ± 161	44.02 ± 0.29	7.51 ± 0.50	14.92 ± 1.47	5.9
SDSS0924+0219	Hβ	1990 ± 210	44.02 ± 0.29	7.35 ± 0.10	14.64 ± 2.17	3.9
Q1017−207	Hα	6177 ± 925	45.74 ± 0.44	9.55 ± 1.18	16.28 ± 0.10	5.5
HE1104−1805	Hα	3972 ± 226	45.28 ± 0.73	8.87 ± 0.70	15.83 ± 0.33	18.5
SDSS1138+0314	Hα	2330 ± 138	44.57 ± 0.31	7.95 ± 0.50	15.21 ± 1.47	10.8
LBQS1333+0113	Hα	4337 ± 140	45.48 ± 0.48	9.08 ± 0.60	15.97 ± 0.39	5.72
WFI2026−4536	Hα	2344 ± 15	45.07 ± 0.53	8.28 ± 0.25	15.43 ± 0.77	6.9
WFI2026−4536	Hβ	1588 ± 168	45.07 ± 0.53	7.83 ± 0.35	14.96 ± 0.63	4.9
WFI2033−4723	Hα	2684 ± 254	44.82 ± 0.15	8.23 ± 0.23	15.40 ± 0.81	4.29
HE2149−2745	Hα	4205 ± 272	45.88 ± 0.59	9.31 ± 0.93	16.12 ± 0.20	5.55
X-shooter						
QJ0158−4325						
A	CIV	4880.26 ± 166.63	44.49 ± 0.92	8.02 ± 0.21	14.42 ± 0.85	11.06
	MgII	4069.70 ± 92.59	44.59 ± 0.45	8.50 ± 0.11	15.09 ± 1.13	18.74
	Hα	4865.23 ± 129.42	44.20 ± 0.46	8.34 ± 0.22	15.47 ± 0.83	9.63
B	CIV	5164.00 ± 334.75	44.48 ± 0.87	8.07 ± 0.54	14.46 ± 0.44	2.63
	MgII	4204.90 ± 204.77	44.56 ± 0.91	8.51 ± 0.24	15.10 ± 0.79	7.44
	Hα	4651.04 ± 232.36	44.18 ± 0.90	8.30 ± 0.47	15.45 ± 0.51	5.80
SDSS1226−0006						
A	MgII	5337.24 ± 205.29	44.94 ± 0.54	8.95 ± 0.34	15.39 ± 0.64	6.8
B	MgII	5331.44 ± 133.12	44.81 ± 0.89	8.87 ± 0.96	15.33 ± 0.69	4.00
LBQS1333+0113						
A	MgII	4521.71 ± 69.38	45.88 ± 0.49	9.38 ± 0.15	15.67 ± 1.00	15.80
	Hα	4608.55 ± 69.73	45.48 ± 0.48	9.13 ± 0.54	16.00 ± 0.44	8.47
B	MgII	4508.73 ± 29.97	45.45 ± 0.93	9.12 ± 0.48	15.51 ± 0.50	8.79
	Hα	4754.73 ± 23.66	45.06 ± 0.94	8.88 ± 0.98	15.84 ± 0.59	8.56
Q1355−2257						
A	CIV	2939.65 ± 254.82	45.68 ± 0.95	8.29 ± 0.18	14.60 ± 0.92	9.69
	MgII	4254.30 ± 74.41	45.78 ± 0.88	9.26 ± 0.13	15.59 ± 1.06	23.34
	Hα	3620.07 ± 65.09	45.39 ± 0.88	8.86 ± 0.70	15.82 ± 0.33	23.84
B	CIV	2702.83 ± 120.74	45.49 ± 0.97	8.11 ± 0.77	14.50 ± 0.98	3.41
	MgII	4118.03 ± 106.32	45.57 ± 0.95	9.11 ± 0.32	15.50 ± 1.15	10.40
	Hα	3442.36 ± 108.17	45.17 ± 0.95	8.68 ± 0.53	15.70 ± 0.45	14.14
FORS2						
SDSS1226−0006						
A	MgII	4760.49 ± 295.07	44.94 ± 0.54	8.85 ± 0.45	15.32 ± 0.52	8.8
B	MgII	4838.84 ± 316.89	44.81 ± 0.89	8.79 ± 0.69	15.28 ± 0.49	10.17

Notes. [a] $L_{\rm ref}$ = Luminosity (L_{1450}, L_{3000} , L_{5100}, L_{5100}) for CIV, MgII, Hα, and Hβ, respectively. All of them are obtained from the SEDs. [b] $r_{\rm s}$ is the accretion disk size obtained from Eq. (3) of Mosquera & Kochanek (2011) at the $\lambda_{\rm rest}$ of the emission line used for the $M_{\rm BH}$ measurement.

color in Fig. 8). The MgII measurement from Sluse et al. (2012) ($\log_{10}(M_{\rm BH}/M_\odot) = 9.04 \pm 0.34$) agrees with our estimate using the same line. As in the previous case, the CIV emission line for QJ0158−4325 is not consistent with the other estimates. The mean values for MgII and Hα are $\log_{10}(M_{\rm BH}/M_\odot) = 8.51 \pm 0.27$ and $\log_{10}(M_{\rm BH}/M_\odot) = 8.32 \pm 0.52$, respectively.

We were also able to estimate the unlensed size of the quasar accretion disk, $r_{\rm s}$ (Eq. (3) of Mosquera & Kochanek 2011) using our $M_{\rm BH}$ estimates and assuming a thin disk model (Shakura & Sunyaev 1973). The details of the parameters used are in Melo et al. (2021) and the size estimates are shown in Table 3. SDSS0924+0219 has the smallest accretion disk size (mean value between Hα and Hβ emission line of $r_{\rm s} = 10^{14.78\pm2.62}$ cm, an error in dex of 5.99. These spectra had very low signal-to-noise (∼5.9 and ∼3.9 in Hα and Hβ lines, respectively). The mean value for the systems QJ0158−4325, SDSS1226−0006, LBQS1333+0113 and Q1355−2257 (all emission lines from both images excluding CIV are $10^{15.28\pm1.28}$ cm, $10^{15.33\pm1.18}$ cm $10^{15.76\pm0.89}$ cm and $10^{15.65\pm1.13}$ cm, respectively.

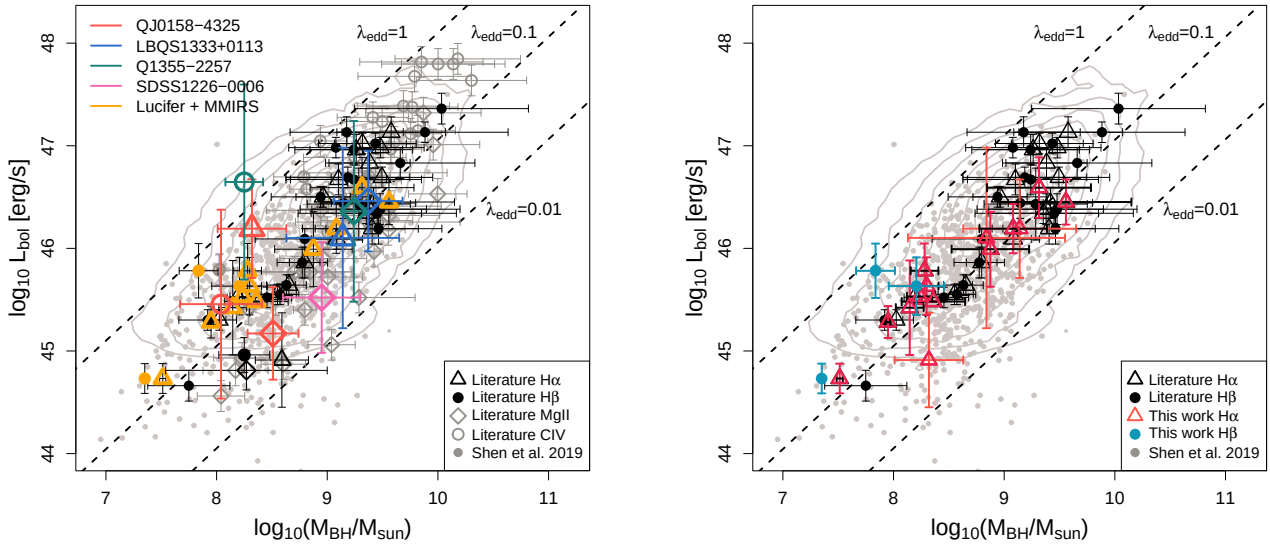

Fig. 8. Logarithmic $M_{\rm BH}$ and bolometric luminosity. Left: for all available lensed quasars (Greene et al. 2010; Sluse et al. 2012; Assef et al. 2011; Peng et al. 2006; Melo et al. 2021) and for non-lensed quasars from Shen et al. (2011, 2019). The open triangles are the $M_{\rm BH}$ estimates using Hα emission line, filled circles Hβ, open diamonds MgII, and open circles CIV. The measurements from this study are in color. Right: for just the Hα and Hβ emission lines. The red and blue points are our estimates. The dashed lines correspond to Eddington ratios of λ = 1, 0.1, and 0.01.

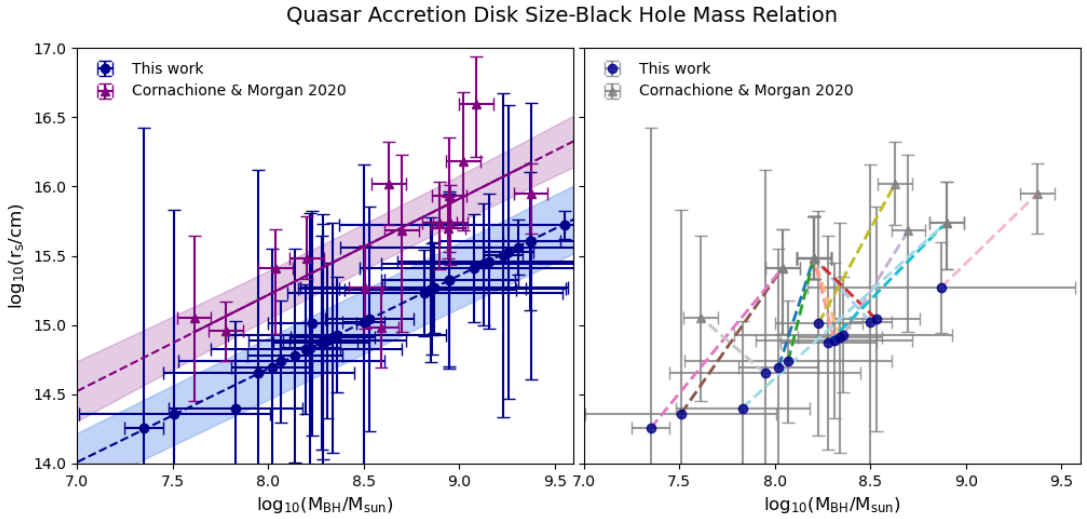

Fig. 9. Quasar accretion disk size-BH mass relation compared to that from Cornachione & Morgan (2020). Left: sample of lensed quasars rescaling our $r_{\rm s}$ values to 2500 Å. A single power-law line is fitted to both samples. Right: same as the left panel but including only those sources common to both samples. The lines connect estimates for the same object. In some cases, the Cornachione & Morgan (2020) target is linked to two $M_{\rm BH}$ estimates based on different emission lines (e.g., Hα and Hβ for SDSS1138+0314).

Our $r_{\rm s}$ estimates can be compared to the accretion disk sizes derived from microlensing using multi-epoch light curves (Cornachione & Morgan 2020, see our Fig. 9). We rescaled our $r_{\rm s}$ to 2500 Å, the wavelength used by Cornachione & Morgan (2020), by assuming the relation $r_{\rm s} \propto \lambda^{4/3}$. While our uncertainties are larger, our results qualitatively agree with the conclusion of Cornachione & Morgan (2020), that microlensing radii are larger (∼0.5 dex) than expected from thin disk theory. In the right panel of Fig. 9 we show the $M_{\rm BH}$ for those systems that are in both samples (seven). The BH mass estimates of the two studies differ for the same sample of objects, with the estimates in Cornachione & Morgan (2020) being higher than ours (except for SDSS1138+0314 and the MgII based estimate for QJ0158−4325), albeit generally within the error bars. Since the BH masses in Cornachione & Morgan (2020) are also estimated using the SE method, the differences must come from the exact prescriptions used to estimate them. Figure 9 shows, however, that the differences in $r_{\rm s}$ are not driven by the difference in the BH estimates.

5. Conclusions

We estimated $M_{\rm BH}$ using the broad Balmer emission lines of 14 lensed quasars measured using four different spectrographs (LUCI, MMIRS, X-shooter, and FORS2). After reducing and extracting the spectra corresponding to each image, the FWHMs of the BELs were estimated using the standard deviation of the model line profile after subtracting the narrow line components. The monochromatic luminosities were estimated using the demagnified SED of the brightest image, taking the variability (if any) into account in the uncertainty budget.

These are the first $M_{\rm BH}$ estimates for the systems QJ0158−4325, HE0512−3329, and WFI2026−4536. We also calculated $M_{\rm BH}$ using the MgII emission line for the systems QJ0158−4325, SDSS1226−0006, LBQS13333+0113, and Q1355−2257.

We compared the new $M_{\rm BH}$ Balmer line to previous MgII $M_{\rm BH}$ estimates for HE0047−1756, HE0435−1223, SDSS0924+0219, SDSS1226−0006, LBQS1333+0113, Q1355−2257, and WFI2033−4723. The mass estimates are well correlated, with the exception of three lensed quasars (FBQ0951+2635, B1422+231, and Q2237+030), whose Balmer masses were not derived here.

The new Balmer $M_{\rm BH}$ span the same range of mass estimates as non-lensed quasars, with the systems QJ0158−4325, SDSS0924+0219, HE0512−3329, and HE0047−1756 having the lowest luminosities. Three systems observed with X-shooter (QJ0158−4325, LBQS13333+0113, and Q1355−2257) were analyzed in detail because they have multiple $M_{\rm BH}$ estimates based off different emission lines. The masses of the lensed quasars imply low Eddington ratios (∼0.1), in agreement with the results of Shen et al. (2019) from SE BH masses of SDSS quasars. Our $M_{\rm BH}$ estimations are also consistent with those obtained from microlensing by Cornachione & Morgan (2020).

A decade after the initial BH mass measurements for gravitational lens systems (Peng et al. 2006; Greene et al. 2010; Assef et al. 2011; Sluse et al. 2012), this work expands the sample from 14 to 23 mass estimates. The $M_{\rm BH}$ measurements of lensed quasars based on the Balmer lines show a lower dispersion in $M_{\rm BH}$ ($RMS \sim 0.45$ dex) at fixed bolometric luminosity, which is also true of non-lensed quasars (Shen et al. 2019). Including the MgII estimates increases the dispersion ($RMS \sim 0.65$ dex), confirming that the Balmer lines are more reliable. An even larger dispersion is observed when the MgII lens $M_{\rm BH}$ estimates from the literature are included. The recent discovery of new gravitational lens systems (Lemon et al. 2023) will allow us to explore the low-luminosity region.

Acknowledgements. We thank Kelly Denney for help with the experimental design of the LUCI and MMIRS observations. We thank Franz Bauer and Ezequiel Treister for carrying out the MMIRS observations. We thank Daniela Zúñiga Sacks for help with the reduction of the LUCI data. R.J.A. was supported by FONDECYT grant number 1231718 and by the ANID BASAL project FB210003. V.M. acknowledges support from ANID FONDECYT Regular grant number 1231418 and Centro de Astrofísica de Valparaíso. N.G. acknowledges support by ANID, Millennium Science Initiative Program – NCN19_171. This project has received funding from the European Research Council (ERC) under the European Union's Horizon Europe research and innovation programme (ESCAPE, grant agreement No 101044152). The LBT is an international collaboration among institutions in the United States, Italy and Germany. LBT Corporation partners are: The University of Arizona on behalf of the Arizona university system; Istituto Nazionale di Astrofisica, Italy; LBT Beteiligungsgesellschaft, Germany, representing the Max-Planck Society, the Astrophysical Institute Potsdam, and Heidelberg University; The Ohio State University, and The Research Corporation, on behalf of The University of Notre Dame, University of Minnesota and University of Virginia.

References

Antonucci, R. 1993, ARA&A, 31, 473
Assef, R. J., Kochanek, C. S., Brodwin, M., et al. 2010, ApJ, 713, 970
Assef, R. J., Denney, K. D., Kochanek, C. S., et al. 2011, ApJ, 742, 93
Barth, A. J., Bennert, V. N., Canalizo, G., et al. 2015, ApJS, 217, 26
Baskin, A., & Laor, A. 2005, MNRAS, 356, 1029
Bate, N. F., Vernardos, G., O'Dowd, M. J., et al. 2018, MNRAS, 479, 4796
Bentz, M. C., Peterson, B. M., Pogge, R. W., Vestergaard, M., & Onken, C. A. 2006, ApJ, 644, 133
Bentz, M. C., Peterson, B. M., Netzer, H., Pogge, R. W., & Vestergaard, M. 2009, ApJ, 697, 160
Bhatiani, S., Dai, X., & Guerras, E. 2019, ApJ, 885, 77
Bonvin, V., Courbin, F., Suyu, S. H., et al. 2017, MNRAS, 465, 4914
Braibant, L., Hutsemékers, D., Sluse, D., Anguita, T., & García-Vergara, C. J. 2014, A&A, 565, L11
Bujarrabal, V., Guibert, J., & Balkowski, C. 1981, A&A, 104, 1
Chilingarian, I., Beletsky, Y., Moran, S., et al. 2015, PASP, 127, 406
Coatman, L., Hewett, P. C., Banerji, M., & Richards, G. T. 2016, MNRAS, 461, 647
Coatman, L., Hewett, P. C., Banerji, M., et al. 2017, MNRAS, 465, 2120
Collin, S., Kawaguchi, T., Peterson, B. M., & Vestergaard, M. 2006, A&A, 456, 75
Cornachione, M. A., & Morgan, C. W. 2020, ApJ, 895, 93
Croton, D. J., Springel, V., White, S. D. M., et al. 2006, MNRAS, 365, 11
Deeming, T. J. 1964, MNRAS, 127, 493
Di Matteo, T., Springel, V., & Hernquist, L. 2005, Nature, 433, 604
Ding, X., Liao, K., Treu, T., et al. 2017a, MNRAS, 465, 4634
Ding, X., Treu, T., Suyu, S. H., et al. 2017b, MNRAS, 472, 90
Ding, X., Treu, T., Birrer, S., et al. 2021, MNRAS, 501, 269
Du, P., Lu, K.-X., Hu, C., et al. 2016, ApJ, 820, 27
Eigenbrod, A., Courbin, F., Meylan, G., Vuissoz, C., & Magain, P. 2006, A&A, 451, 759
Falco, E. E., Kochanek, C. S., Lehár, J., et al. 2001, ASP Conf. Ser., 237, 25
Ferrarese, L., & Merritt, D. 2000, ApJ, 539, L9
Fian, C., Guerras, E., Mediavilla, E., et al. 2018a, ApJ, 859, 50
Fian, C., Mediavilla, E., Jiménez-Vicente, J., Muñoz, J. A., & Hanslmeier, A. 2018b, ApJ, 869, 132
Francis, P. J., & Wills, B. J. 1999, ASP Conf. Ser., 162, 363
Freudling, W., Romaniello, M., Bramich, D. M., et al. 2013, A&A, 559, A96
Giannini, E., Schmidt, R. W., Wambsganss, J., et al. 2017, A&A, 597, A49
Greene, J. E., & Ho, L. C. 2005, ApJ, 630, 122
Greene, J. E., Peng, C. Y., & Ludwig, R. R. 2010, ApJ, 709, 937
Grier, C. J., Trump, J. R., Shen, Y., et al. 2017, ApJ, 851, 21
Grier, C. J., Shen, Y., Horne, K., et al. 2019, ApJ, 887, 38
Guerras, E., Dai, X., & Mediavilla, E. 2020, ApJ, 896, 111
Hopkins, P. F., Hernquist, L., Cox, T. J., & Kereš, D. 2008, ApJS, 175, 356
Hutsemékers, D., & Sluse, D. 2021, A&A, 654, A155
Inada, N., Becker, R. H., Burles, S., et al. 2003, AJ, 126, 666
Inada, N., Oguri, M., Becker, R. H., et al. 2008, AJ, 135, 496
Kaspi, S., Smith, P. S., Netzer, H., et al. 2000, ApJ, 533, 631
Kaspi, S., Maoz, D., Netzer, H., et al. 2005, ApJ, 629, 61
Kausch, W., Noll, S., Smette, A., et al. 2015, A&A, 576, A78
Kochanek, C. S. 2004, ApJ, 605, 58
Kormendy, J., & Ho, L. C. 2013, ARA&A, 51, 511
Kormendy, J., & Richstone, D. 1995, ARA&A, 33, 581
Lemon, C., Anguita, T., Auger-Williams, M. W., et al. 2023, MNRAS, 520, 3305
Lira, P., Kaspi, S., Netzer, H., et al. 2018, ApJ, 865, 56
Malik, U., Sharp, R., Penton, A., et al. 2023, MNRAS, 520, 2009
Marconi, A., & Hunt, L. K. 2003, ApJ, 589, L21
Marziani, P., Sulentic, J. W., Plauchu-Frayn, I., & del Olmo, A. 2013, A&A, 555, A89
McGill, K. L., Woo, J.-H., Treu, T., & Malkan, M. A. 2008, ApJ, 673, 703
McLeod, B., Fabricant, D., Nystrom, G., et al. 2012, PASP, 124, 1318
McLure, R. J., & Dunlop, J. S. 2004, MNRAS, 352, 1390
McLure, R. J., & Jarvis, M. J. 2002, MNRAS, 337, 109
Mediavilla, E., & Jiménez-Vicente, J. 2021, ApJ, 914, 112
Mediavilla, E., Muñoz, J. A., Falco, E., et al. 2009, ApJ, 706, 1451
Mediavilla, E., Jiménez-vicente, J., Mejía-restrepo, J., et al. 2020, ApJ, 895, 111
Mejía-Restrepo, J. E., Trakhtenbrot, B., Lira, P., Netzer, H., & Capellupo, D. M. 2016, MNRAS, 460, 187
Mejía-Restrepo, J. E., Trakhtenbrot, B., Lira, P., & Netzer, H. 2018, MNRAS, 478, 1929
Melo, A., Motta, V., Godoy, N., et al. 2021, A&A, 656, A108
Morgan, N. D., Dressler, A., Maza, J., Schechter, P. L., & Winn, J. N. 1999, AJ, 118, 1444
Morgan, N. D., Gregg, M. D., Wisotzki, L., et al. 2003, AJ, 126, 696
Morgan, N. D., Caldwell, J. A. R., Schechter, P. L., et al. 2004, AJ, 127, 2617
Morgan, C. W., Kochanek, C. S., Morgan, N. D., & Falco, E. E. 2010, ApJ, 712, 1129
Mosquera, A. M., & Kochanek, C. S. 2011, ApJ, 738, 96
Muñoz, J. A., Mediavilla, E., Kochanek, C. S., Falco, E. E., & Mosquera, A. M. 2011, ApJ, 742, 67
Netzer, H., & Peterson, B. M. 1997, Astrophys. Space Sci. Lib., 218, 85
Netzer, H., & Trakhtenbrot, B. 2007, ApJ, 654, 754
Oguri, M., Inada, N., Castander, F. J., et al. 2004, PASJ, 56, 399
Park, D., Woo, J.-H., Denney, K. D., & Shin, J. 2013, ApJ, 770, 87
Park, D., Woo, J.-H., Bennert, V. N., et al. 2015, ApJ, 799, 164
Peng, C. Y., Impey, C. D., Rix, H.-W., et al. 2006, ApJ, 649, 616
Peterson, B. M. 1993, PASP, 105, 247

Peterson, B. M. 2014, Space. Sci. Rev., 183, 253
Peterson, B. M., Ferrarese, L., Gilbert, K. M., et al. 2004, ApJ, 613, 682
Poindexter, S., Morgan, N., Kochanek, C. S., & Falco, E. E. 2007, ApJ, 660, 146
Ricci, D., Poels, J., Elyiv, A., et al. 2011, A&A, 528, A42
Rojas, K., Motta, V., Mediavilla, E., et al. 2014, ApJ, 797, 61
Rupprecht, G., & Böhnhardt, H. 2000, FORS1+ 2 User Manual V1. 4, Tech. rep., VLT-MAN-ESO-13100-1543
Seifert, W., Appenzeller, I., Baumeister, H., et al. 2003, Proc. SPIE, 4841, 962
Shakura, N. I., & Sunyaev, R. A. 1973, A&A, 500, 33
Shen, Y. 2013, Bull. Astron. Soc. India, 41, 61
Shen, Y., & Liu, X. 2012, ApJ, 753, 125
Shen, Y., Greene, J. E., Strauss, M. A., Richards, G. T., & Schneider, D. P. 2008, ApJ, 680, 169
Shen, Y., Richards, G. T., Strauss, M. A., et al. 2011, ApJS, 194, 45
Shen, Y., Grier, C. J., Horne, K., et al. 2019, ApJ, 883, L14
Shen, Y., Grier, C. J., Horne, K., et al. 2023, ArXiv e-prints [arXiv:2305.01014]
Sluse, D., Hutsemékers, D., Courbin, F., Meylan, G., & Wambsganss, J. 2012, A&A, 544, A62
Smette, A., Sana, H., Noll, S., et al. 2015, A&A, 576, A77
Tremaine, S., Gebhardt, K., Bender, R., et al. 2002, ApJ, 574, 740
Urry, C. M., & Padovani, P. 1995, PASP, 107, 803
Vacca, W. D., Cushing, M. C., & Rayner, J. T. 2003, PASP, 115, 389
Vernet, J., Dekker, H., D'Odorico, S., et al. 2011, A&A, 536, A105
Vestergaard, M. 2002, ApJ, 571, 733
Vestergaard, M. 2004, ApJ, 601, 676
Vestergaard, M., & Peterson, B. M. 2006, ApJ, 641, 689
Wandel, A., Peterson, B. M., & Malkan, M. A. 1999, ApJ, 526, 579
Wang, J.-G., Dong, X.-B., Wang, T.-G., et al. 2009, ApJ, 707, 1334
Wisotzki, L., Schechter, P. L., Bradt, H. V., Heinmüller, J., & Reimers, D. 2002, A&A, 395, 17
Woo, J.-H., Yoon, Y., Park, S., Park, D., & Kim, S. C. 2015, ApJ, 801, 38
Woo, J.-H., Le, H. A. N., Karouzos, M., et al. 2018, ApJ, 859, 138
Xiao, T., Barth, A. J., Greene, J. E., et al. 2011, ApJ, 739, 28
Yu, Z., Martini, P., Penton, A., et al. 2023, MNRAS, 522, 4132
Zu, Y., Kochanek, C. S., & Peterson, B. M. 2011, ApJ, 735, 80
Zubovas, K., & King, A. R. 2019, Gen. Rel. Grav., 51, 65

Appendix A: Table of magnitudes

Table A.1. Magnitudes for images A and B (for five lensed quasars: QJ0158−4325, SDSS1226−0006, LBQS1333−0113, and Q1355−2257) of each system used for constructing the SED.

System	Instrument	Filter	Magnitude [mag]	Ref.
HE0047−1756	HST[1]	F160W	15.33 ± 0.02	CASTLES[2]
	HST	F555W	17.57 ± 0.18	CASTLES
	HST	F814W	16.86 ± 0.15	CASTLES
	Gaia	*Gaia* DR1	16.542 ± 0.2	GLQ Database[3]
QJ0158−4325	HST	F160W	16.47 ± 0.03	CASTLES
image A	HST	F555W	18.10 ± 0.13	CASTLES
	HST	F814W	17.81 ± 0.04	CASTLES
	du Pont	R	17.338 ± 0.001	Morgan et al. (1999)
	HST	F160W	17.27 ± 0.03	CASTLES
image B	HST	F555W	18.91 ± 0.17	CASTLES
	HST	F814W	18.62 ± 0.11	CASTLES
	du Pont[4]	R	18.487 ± 0.004	Morgan et al. (1999)
HE0435−1223	HST	F160W	17.31 ± 0.02	CASTLES
	HST	F555W	18.58 ± 0.02	CASTLES
	HST	F814W	17.84 ± 0.02	CASTLES
	MagIC[5]	g	19.00	Wisotzki et al. (2002)
	MagIC	r	18.44	Wisotzki et al. (2002)
HE0512−3329	HST	F160W	15.81 ± 0.02	CASTLES
	HST	F220W	18.96 ± 0.11	Muñoz et al. (2011)
	HST	F250W	18.07 ± 0.23	Muñoz et al. (2011)
	HST	F330W	17.67 ± 0.13	Muñoz et al. (2011)
	HST	F435W	18.67 ± 0.03	Muñoz et al. (2011)
	HST	F555W	18.10 ± 0.05	Muñoz et al. (2011)
	HST	F625W	17.60 ± 0.05	Muñoz et al. (2011)
	HST	F814W	16.98 ± 0.03	Muñoz et al. (2011)
SDSS0924+0219	HST	F160W	17.96 ± 0.02	CASTLES
	HST	F555W	19.61 ± 0.01	CASTLES
	HST	F814W	18.75 ± 0.05	CASTLES
	SDSS[6]	u	19.66 ± 0.02	Inada et al. (2003)
	SDSS	g	19.46 ± 0.01	Inada et al. (2003)
	SDSS	r	18.97 ± 0.01	Inada et al. (2003)
	SDSS	i	18.87 ± 0.02	Inada et al. (2003)
Q1017−207	HST	F160W	15.66 ± 0.03	CASTLES
	HST	F555W	17.43 ± 0.03	CASTLES
	HST	F814W	16.92 ± 0.02	CASTLES
HE1104−1805	HST	F160W	15.91 ± 0.01	CASTLES
	HST	F555W	16.92 ± 0.06	CASTLES
	HST	F814W	16.40 ± 0.03	CASTLES
	Spitzer	IRAC 3.6	14.03 ± 0.04	Poindexter et al. (2007)
	Spitzer	IRAC 4.5	13.285 ± 0.07	Poindexter et al. (2007)
	Spitzer	IRAC 5.8	12.195 ± 0.03	Poindexter et al. (2007)
	Spitzer	IRAC 8.0	10.87 ± 0.03	Poindexter et al. (2007)
SDSS1226−0006	HST	F160W	17.24 ± 0.02	CASTLES
image A	HST	F555W	18.57 ± 0.01	CASTLES
	HST	F814W	18.84 ± 0.10	CASTLES
	SDSS	i	18.23	Inada et al. (2008)
	HST	F160W	18.01 ± 0.02	CASTLES
image B	HST	F555W	19.33 ± 0.03	CASTLES
	HST	F814W	19.36 ± 0.07	CASTLES
	Gaia	*Gaia* DR1	19.241	GLQ Database
SDSS1138+0314	HST	F160W	17.96 ± 0.02	CASTLES
	HST	F555W	19.37 ± 0.07	CASTLES
	HST	F814W	19.05 ± 0.01	CASTLES
	Gaia	*Gaia* DR2	19.683	GQL Database

Table A.1. continued.

System	Instrument	Filter	Magnitude [mag]	Ref.
LBQS1333+0113	HST	F160W	16.18 ± 0.02	CASTLES
Image A	SDSS	u	18.54	Oguri et al. (2004)
	SDSS	g	18.12	Oguri et al. (2004)
	SDSS	r	17.95	Oguri et al. (2004)
	SDSS	i	17.60	Oguri et al. (2004)
	SDSS	z	17.49	Oguri et al. (2004)
	HST	F160W	17.49 ± 0.02	CASTLES
Image B	SDSS	u	19.68	Oguri et al. (2004)
	SDSS	g	19.39	Oguri et al. (2004)
	SDSS	r	19.09	Oguri et al. (2004)
	SDSS	i	19.68	Oguri et al. (2004)
	SDSS	z	20.05	Oguri et al. (2004)
Q1355−2257	HST	F160W	15.91 ± 0.02	CASTLES
Image A	HST	F555W	17.61 ± 0.12	CASTLES
	HST	F814W	17.21 ± 0.07	CASTLES
	MagIC	g	17.707	Morgan et al. (2003)
	MagIC	r	17.322	Morgan et al. (2003)
	MagIC	i	17.338	Morgan et al. (2003)
	MagIC	z	17.427	Morgan et al. (2003)
	HST	F160W	17.38 ± 0.02	CASTLES
Image B	HST	F555W	19.27 ± 0.14	CASTLES
	HST	F814W	18.57 ± 0.08	CASTLES
	MagIC	g	19.580	Morgan et al. (2003)
	MagIC	r	18.994	Morgan et al. (2003)
	MagIC	i	19.032	Morgan et al. (2003)
	MagIC	z	19.145	Morgan et al. (2003)
WFI2026−4536	HST	F160W	15.64 ± 0.01	CASTLES
	MagIC	i	17.109	Morgan et al. (2004)
	PANIC[7]	Ks	14.978	Morgan et al. (2004)
WFI2033−4723	HST	F160W	17.22 ± 0.02	CASTLES
	HST	F555W	19.24 ± 0.03	CASTLES
	HST	F814W	18.15 ± 0.05	CASTLES
	MagIC	i	18.68 ± 0.01	Morgan et al. (2004)
HE2149−2745	HST	F160W	15.67 ± 0.03	CASTLES
	HST	F555W	16.97 ± 0.03	CASTLES
	HST	F814W	16.52 ± 0.01	CASTLES
	Gaia	*Gaia* DR2	17.003	GQL Database

Notes. [(1)]*Hubble* Space Telescope; [(2)]Falco et al. 2001, https://lweb.cfa.harvard.edu/castles/; [(3)]Gravitationally Lensed Quasar Database, https://research.ast.cam.ac.uk/lensedquasars/index.html; [(4)]du Pont 2.5m telescope at Las Campanas Observatory. [(5)]*Magellan* Instant Camera at Las Campanas Observatory. [(6)]Sloan Digital Sky Survey. [(7)]Persson's Auxiliary Nasmyth Infrared Camera at the *Magellan* Baade telescope.